Performance improvement in a Proton exchange membrane fuel cell with an innovative flow field design

Zhenyu Huang[a], Lu Xing[b, *], Zhengkai Tu [a, *]

[a]School of Energy and Power Engineering, Huazhong University of Science and Technology, Wuhan, 430074, China

[b]Mechanical and Construction Engineering, Northumbria University, Newcastle upon Tyne, NE1 8ST, United Kingdom

*Corresponding author: lu.xing@northumbria.ac.uk; tzklq@hust.edu.cn.

Abstract:

The flow field of the proton exchange membrane fuel cell (PEMFC) controls mass and water transfer; it significantly impacts the fuel cell's performance. It is critical to innovate the flow field design for optimizing the performance. This paper proposes a new-designed flow field (NDFF) patterned with the built-in blockage and trap-shape rib association. The novel design was analyzed numerically and experimentally. A three-dimensional isothermal numerical model was first established based on COMSOL software. This model demonstrated that the NDFF transformed the traditional diffusion mass transfer into the optimized diffusion and convection mass transfer combination. Compared with the conventional straight flow field, the effective mass transfer coefficient was considerably improved. Moreover, the new-designed structures enforced cyclical variation of local velocity and pressure, forming forced-convection, which was beneficial for water management. At 0.45A·cm^{-2}, the steady-state voltage and the initial dynamic response voltage were increased by 0.08V and 0.16V; power density was increased by 20.1%. The experimental results were collected to validate the enhanced performance of PEMFC with the NDFF. Energy efficiency ratio (EER) was proposed as an evaluation criterion; EER results suggested NDFF can improve the net output power.

Keywords: Proton exchange membrane fuel cell; Flow field; Oxygen and water distribution; Energy efficiency ratio

1 Introduction

Climate change caused by environmental pollution and global warming is getting great attention; PEMFCs demonstrated outstanding potential for their advantage of zero-pollution [1-3]. Significant progress has been achieved in developing PEMFC's technologies; however, the cost is still one main obstacle that restricts the large-scale commercialization [4].

The cost can be reduced by improving PEMFC's performance [5]. Flow field significantly affects a fuel cell's performance, whose difference among PEMFCs with different flow fields can reach more than 50% [6]. Researchers have long been committed to flow field optimization to improve PEMFCs' performance [7]. Enhanced mass transfer capacity and water management capacity contribute to improved performance of the PEMFC with a better flow field design. Built-in blockage in the flow channel is a common and effective method for flow field optimization. Ghanbarian et al. [8] concluded that trapezoid blockage can guide the reaction gas to produce the biggest partial velocity in the mass transfer direction and thus the maximum improvement of net output power was obtained. Shen et al. [10] explored the effects of the spacing distance of blockages in flow fields and introduced field synergy theory to explain PEMFC’s performance improvement. Additionally, the concentration loss aroused by insufficient mass transfer can be avoided by increasing the direct contact area between reactant gas and gas diffusion layer. Rezazadeh et al. [12] investigated the flow field shape on the performance of PEMFC. A well-designed flow field can accelerate the discharge of water inside the fuel cell. Li et al. found that waved flow

fields patterned with periodic semi-circle obstacles can introduce enhanced forced-convection, which was beneficial for removing the liquid water in the microstructure. Liu et al. [17] designed a new turn for the serpentine flow field which can partially change the momentum direction of the droplet and make it easier to flow out of the fuel cell under air purging. Baik et al. [18] constructed a new type of metal bipolar plates with multi-holes on ribs of the traditional trapezoid flow field. This design can solve the problem that liquid water under the rib accumulates and cannot be discharged. The holes located on the rib are also beneficial for the mass transfer of reactant gas. Because the newly designed metal bipolar had a smaller low-frequency impedance, 37.75% performance improvement was found.

In addition to operating cost, whether PEMFC can operate stably is also an essential criterion for its large-scale commercialization. Dynamic load changing significantly affects its operational stability [21]. Similarly, there are also dynamic performance differences among PEMFCs with varied flow fields. The dynamic characteristics of the straight channel, single-serpentine channel, the three-serpentine channel had been comparatively investigated by Yan et al. [22]. In the low current density area, undershoot of the response voltage was small, and the poorest dynamic performance was found in the straight channel. However, it gradually exhibited the best dynamic performance with the increased current density. Kim et al. [23] stated based on their experiment that the loss of dynamic performance caused by the vacuum effect could be reduced when the single serpentine channel was used. It was because that single serpentine channel had faster outlet velocity than three serpentine channels, and thus

the reactant gas could be supplied in a timelier manner. Furtherly, Yan et al. [24] found that the four-serpentine channel required the longest recovery time under dynamic loading conditions.

As in-built blockage and rib with trap are convenient and effective ways to optimize flow fields, in this paper, we designed a novel 3D flow field with the combination of the above two excellent structures. The PEMFC with a novel flow field design was fabricated; its enhanced performance would be demonstrated and analyzed numerically and experimentally. A novel designed flow field (NDFF) numerical simulation model was developed for predicting performance improvement. The intrinsic mechanism was investigated by exploring the effects of the NDFF on the distribution of oxygen, velocity, water, and pressure. Meanwhile, the energy efficiency ratio (EER) was proposed as the performance evaluation. Finally, the steady-state and dynamic performance of the PEMFC equipped with a conventional straight flow field (CSFF) and NDFF were tested by experiment and compared using the EER value.

2 Model description

2.1 New-designed flow field

The guideline for flow field optimization is to improve its mass transfer capacity and water management ability in cathodic sides because of their apparent impacts imposed on PEMFC's performance [25]. In addition, the simpler structure, lower manufacturing cost, and parasitic power of the CSFF make it competitive in practical engineering applications. It is meaningful to make some improvements for CSFF [26]. Hence, the CSFF was adopted as a research object. Nevertheless, serpentine, and other types of

channels could be used in different applications. It should be mentioned that the concept provided was general and could be applied in other flow fields.

The in-built blockage can affect reactant gas flow in the flow field and generate enhanced secondary flow and crossover flow, promoting more oxygen into the gas diffusion and catalytic layers [27]. The optimization of the rib can suppress the uneven distribution of reactant gas and improve the whole oxygen concentration [12, 28]. The generated water would purge more quickly with a cyclical variation of local velocity and pressure introduced by the NDFF. As exhibited in Fig.1, an optimal new-designed 3D cathodic flow field with the combination of the in-built blockage and trap-shape rib was proposed.

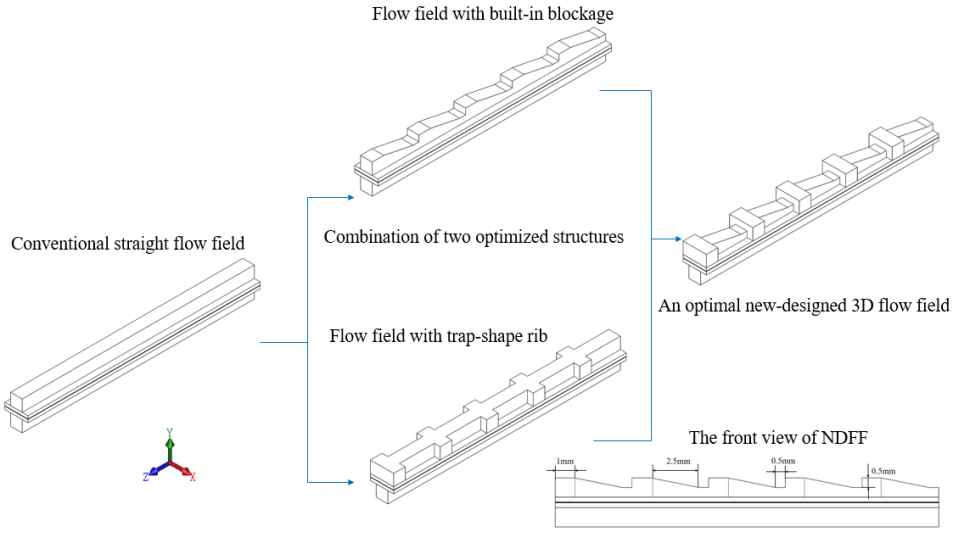

Figure 1: Schematic diagram of the optimized design of NDFF

2.2 Model assumptions

PEMFC is a complex system including electrochemical reaction, transmitting electrons and ions, transferring reactant gas and momentum, and energy transformation in one or more computational domains. Appropriate assumptions were necessary with the premise of ensuring calculation reasonableness because the situation was too

complicated.

1. The working temperature of the fuel cell is set constantly [28].
2. The reactant gas is ideal, and the flow is laminar [29].
3. No interpenetration of hydrogen and oxygen in the electrolyte membrane [29].
4. The materials in membrane assembly electrode (MEA), including proton exchange membrane, catalytic layer, and diffusion layer, are all isotropic [30].
5. The water in the fuel cell is only gas [12, 31, 32].
6. The effects aroused by gravity are ignored [33].

2.3 Computational domain and boundary conditions

2.3.1 Computational domain

The geometric configuration of the three-dimensional isothermal model of the single fuel cell described in Fig.1 was fabricated in SOLIDWORKS software. And then, it was imported into COMSOL software for meshing and multi-physics coupling calculation. When the relative tolerance value of all variables drops below 10^{-3}, the numerical result converges.

2.3.2 Boundary conditions

The inlet of the flow channel adopted an inlet condition named mass flow rate, which is perpendicular to its inlet interface. The magnitude of mass flow rate was calculated based on stoichiometry, temperature, relative humidity, and working current density, which was the same as the experiment. The technical parameters of the fuel cell were listed in Table 1.

(1) The boundary type applied at the inlets on both anode and cathode sides is mass-

flow-inlet. The values of mass fraction and mass flow rate of H_2, O_2, H_2O, and N_2 are prescribed and the mass flow direction is perpendicular to their inlet interface.

(2) The boundary type applied at the outlets on both anode and cathode sides is pressure-outlet. The values of pressure are set to zero as there are no backpressure and the options of the backflow condition are defined.

(3) The no-slip boundary conditions are adapted for the wall regions between the inlets and outlets [34].

(4) The symmetrical boundary conditions are adapted for the gas diffusion layers and catalyst layers cutoff plane to simulate the situation where a single flow channel computational domain was separately extracted from the PEMFC [35].

(5) The electrode phase potential is fixed value as a static potential boundary condition on the external contact boundaries. In this model, the anode electrode phase potential is set to zero, that is $\Phi_s = 0$. And on the cathode side, the electrode phase potential is set to cell voltage, that is $\Phi_s = V_{cell}$.

Table 1: Technical parameters of the fuel cell

Parameter	Value
Flow field width	1 mm
Flow field depth	1 mm
Flow field rib width	1 mm
Gas diffusion layer thickness	0.25 mm
PEM thickness	0.025 mm
Catalyst layer thickness	0.01 mm

Operation pressure	1 atm
Open-circuit voltage	0.98V
operation temperature	323K
Humidification temperature	303K
Stoichiometry of cathode	3
Stoichiometry of anode	1.5

2.4 Governing Equations

The electrochemical model should include the generation, transfer, and conservation of charge. The electrode kinetic equations were used to describe the electrochemical reaction processes in the anodic and cathodic catalyst layer which generated charge. The hydrogen oxidation reaction in the anode catalyst layer and the relationship among different physical quantities during the electrochemical reaction could be described as the linear Butler-Volmer equation [20, 36], as shown in Equation (1):

$$i_a = i_{0,a} \left(\frac{c_{loc,H_2}}{c_{ref,H2}}\right)^{0.5} \left(\frac{\alpha_a + \alpha_c}{RT} F\eta_a\right) \quad (1)$$

The oxygen reduction reaction occurred in the cathodic catalyst layer and the Tafel equation was used duo to the large overpotential[35], as shown in Equation (2):

$$i_c = -i_{0,c}\left(\frac{c_{loc,O_2}}{c_{ref,O_2}}\right) 10^{\eta_c/A_c} \quad (2)$$

Overpotential η_i was a function of electron potential Φ_s, ion potential Φ_l and electrode equilibrium potential φ_i^0[27], as shown in Equation (3):

$$\eta_i = \Phi_s - \Phi_l - \varphi_i^0 \quad (3)$$

There are two kinds of current in a PEMFC: electronic current i_s and ion current i_l.

According to Ohmic law, the relationship to the electron potential and ion potential were listed as follows [30], in Equations (4) and (5).

$$\nabla(-\sigma_s \nabla \Phi_s) = i_s \tag{4}$$

$$\nabla(-\sigma_l \nabla \Phi_l) = i_l \tag{5}$$

The continuity equation of current density can be expressed as shown in Equation (6):

$$\nabla i_s + \nabla i_l = 0 \tag{6}$$

The mass conservation of the reaction gas flowing in the fuel cell can be described in the continuity equation, Equation (7).

$$\nabla \cdot (\rho \vec{u}) = S_i \tag{7}$$

The Navier-Stokes equation was extended to the brinkman equation to make it suitable for the momentum transfer in porous material [35, 37], as shown in Equation (8):

$$\frac{\rho}{\varepsilon}((\vec{u} \cdot \nabla)\frac{\vec{u}}{\varepsilon}) = \nabla \cdot \left[-P + \frac{\mu}{\varepsilon}(\nabla \vec{u} + (\nabla \vec{u})^T - \frac{2\mu}{3\varepsilon}(\nabla \cdot \vec{u})\right] - (\frac{\mu}{K} + S_i)\vec{u} \tag{8}$$

The species conservation of the reactant gas can be described in Equation (9) [38]:

$$\nabla \cdot [-\rho \omega_i \sum_j D_{ij}^{eff} \{\frac{M}{M_j}(\nabla \omega_j + \omega_j \frac{\nabla M}{M}) + \frac{\nabla P}{P}(x_j - \omega_j)\} + \omega_i \rho \vec{u}] = S_i \tag{9}$$

The effective diffusion coefficient D_{ij}^{eff} in the porous material in anode and cathode is calculated with porosity ε [39, 40] as shown in Equation (10):

$$D_{ij}^{eff} = \mathrm{D}_{ij} \varepsilon^{1.5} \tag{10}$$

The density of the mixed gas is a function of the mixture as shown in Equation (11):

$$\rho = (\sum_i x_i M_i) P/(RT) \tag{11}$$

According to the mass conservation, the water mass fraction in the anode and the nitrogen mass fraction in the cathode could be calculated as shown in Equations (12)

and (13):

$$\omega_{H_2O} = 1 - \omega_{H_2} \tag{12}$$

$$\omega_{N_2} = 1 - \omega_{O_2} - \omega_{H_2O} \tag{13}$$

The hydrodynamic equation in PEMFC was coupled with the electrochemical equation; the source terms of hydrogen, oxygen, and water were controlled by the Faraday equation[27, 41] as shown in Equation (14):

$$S_{H_2} = -\frac{i_a}{2F} M_{H_2}, \quad S_{O_2} = \frac{|i_c|}{4F} M_{O_2}, S_{H_2O} = -\frac{|i_c|}{2F} M_{H_2O} \tag{14}$$

3 Experimental

As shown in Fig.2, the cathodic plates with different flow field characteristics were manufactured. The anode flow field plate remained unchanged during the entire test, while the cathode flow field was replaced after a set of tests was completed to study their effects on the performance of the fuel cell. The bipolar plate used in the experiment was provided by Shanghai Hongfeng Co., Ltd., and was carved by a graphite engraving machine according to the drawings. Compared with the traditional direct flow channel, the new 3D flow field l has more flow channel structure features, resulting in a longer processing time, but the total amount of material required for them is the same. Since the use of the new 3D flow field can improve the performance of the PEMFC, it can improve the fuel utilization rate and reduce the operating cost. Meanwhile, the beneficial effect will continue until the end of the PEMFC use. Therefore, performance enhancement can make up for additional manufacturing costs (longer processing time), and the application of new channels has significant engineering value. If considering the structural characteristics of the new channels for metal bipolar plate, the design of

channel depth, channel height, obstacle length, obstacle height, and other structural parameters need to be further optimized to avoid metal plate cracking, which requires further design and development combined with industrial molding software. However, when the design is completed, the metal plate is produced by stamping and forming with a mold, which does not change the amount of material and processing time.

As shown in Fig.2, the cathodic plates with different flow field characteristics were manufactured. The anode flow field plate with the conventional straight flow field remained unchanged during the entire test, while the cathode flow field was replaced after a set of tests was completed to study their effects on the performance of the fuel cell. The sealing groove was machined on the bipolar plates for a sealing ring made of rubber and was 0.5mm higher than the sealing groove. Due to the compressibility of the rubber, to ensure both good contact and the sealing performance. The single fuel cell is composed of a current collecting plate, flow field plate, sealing ring, and membrane electrode assembly, as shown in Fig.2. The membrane electrode assembly was purchased from Wuhan WUT New Energy Co., Ltd. The graphite flow field plate is not suitable to be directly integrated into the circuit because it is brittle, and the copper current collecting plate was used to assemble the single fuel cell. A total of 10 studs were used, and the torque applied on each nut was 50 kgf • cm and was accurately given by the torque wrench (TOHNICHI) to avoid the adverse effects on the fuel cell aroused by uneven stress distribution [42]. After a single fuel cell was assembled, related experiments on the 850e (Hephas Energy Corporation) test system were conducted. This equipment can accurately control the inlet temperature, relative humidity, working

pressure, and flow rate and obtain real-time voltage and current density parameters. The flow rate for reaction gas was determined by stoichiometry at each loaded current density. The relative humidity was given based on the humidification temperature and there was no backpressure applied. Detailed working parameters as shown in Table 1. And the 885-HS electrochemical working station can be used for impedance analysis. Each experiment was repeated at least three times to exclude the influence of chance.

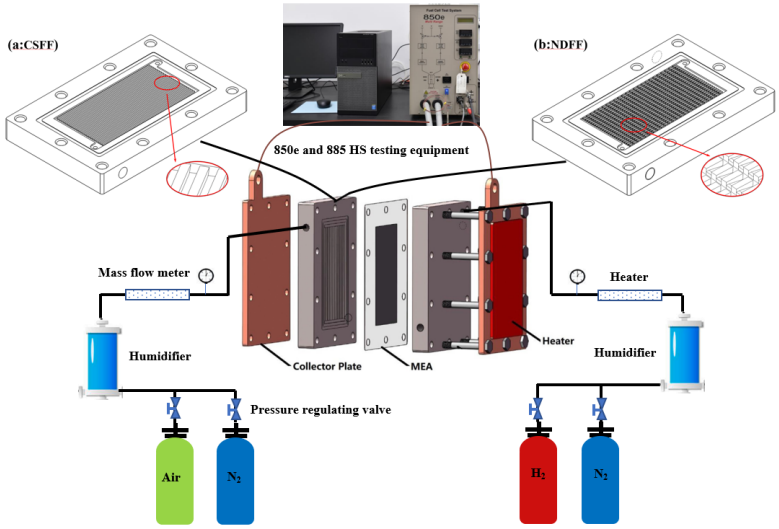

Figure 2: The schematic of the testing single fuel cell and equipment

4 Results and discussion

4.1 Model validation

Fig.3 (a) shows the I-V polarization curves of the CSFF obtained numerically and experimentally. When the fuel cell operates in low current density, the simulation results are greatly consistent with the experimental results. However, performance differences occurred when working current density gradually increased, which could be attributed to the assumption that the water in the fuel cell was all in the form of gas [12, 31]. Therefore, it was necessary to explore the effects of flow fields on the reaction gas and water distribution with simulation and experiment considered together. Finally, as

shown from Fig.3(b), the calculation result was independent of the number of the grid.

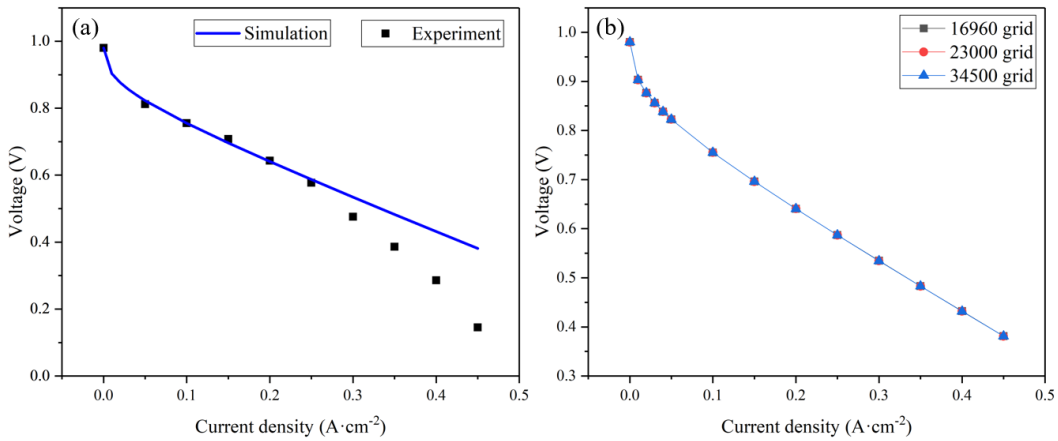

Figure 3: Polarization curves for (a) model validation and (b) grid independence analysis

The oxygen transport has great effects on a fuel cell's performance. A quicker oxygen transport rate means higher oxygen concentration at the membrane electrode assembly and lower reaction kinetics barriers for oxygen reduction, resulting in better fuel cell performance. As the need for oxygen varied for fuel cells working at different currents, the oxygen transport rate is assumed to be of different importance [43]. Fig.4 shows the comparison of simulated polarization curves for various flow fields under the same working conditions. With the continuously increased working current density, the performance improvement of the NDFF gets more pronounced [27]. When it worked at 0.25A·cm^{-2} and 0.45A·cm^{-2}, its voltage was increased by 0.05V and 0.08V, and power density was increased by 8.6% and 20.1%.

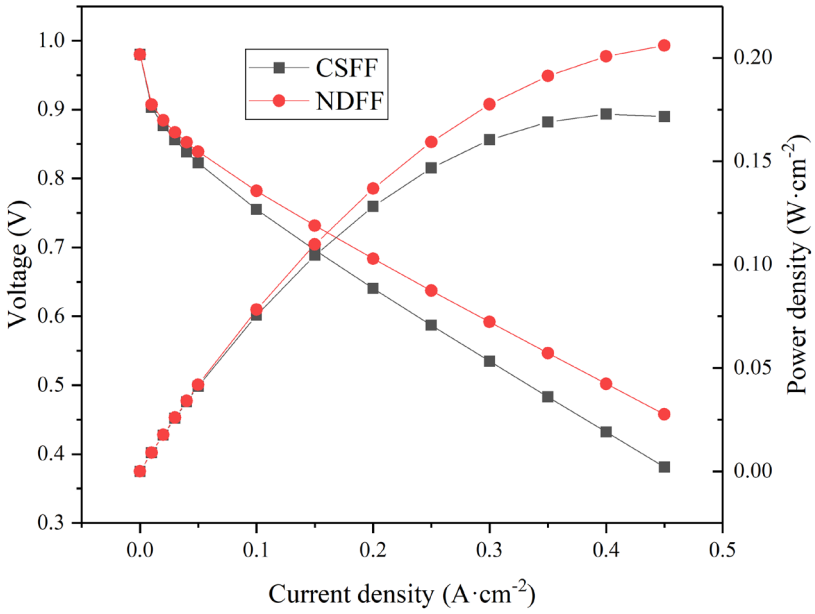

Figure 4: Comparison of simulated polarization curves for different flow fields. (a) CSFF; (b) NDFF

Among different kinds of ohmic loss, the resistance of the proton exchange membrane is the dominant ohmic overpotential in a PEMFC. In addition, the flow channel optimization reduces the contact area between the graphite bipolar plate and the gas diffusion layer. The conductivity of the graphite bipolar plate is 1935S • m^{-1}, and the thickness of the bipolar plate with a reduced contact area is 1mm. The active area of the PEMFC is 50cm, in which the contact area of the ridge and the flow channel is 25cm^2, and the contact area of the bipolar plate due to the improvement of the flow channel is 6.25cm^2. Based on this, it can be calculated that at an operating current density of 0.45A·cm^{-2}, the ohmic loss increased due to the improvement of the bipolar plate is only 0.01861V ($\Delta \boldsymbol{V} = \frac{\mathbf{0.45\times50}}{\mathbf{1.935\times10^{-3}\times6.25\times10^{-4}}}$), which is negligible compared to the performance increase brought by the enhancement of mass transfer

4.2 Oxygen distribution

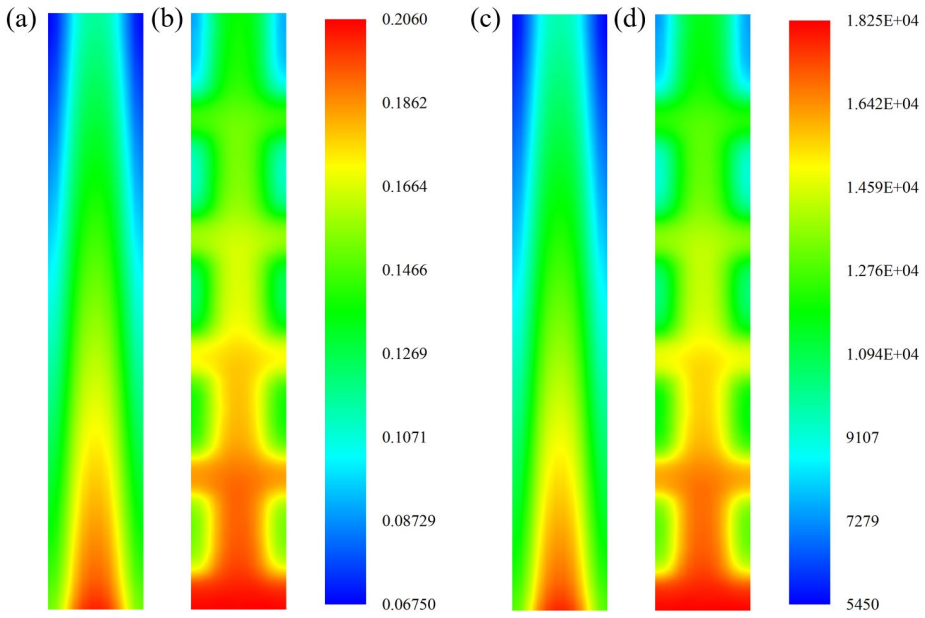

Figure 5: Oxygen distribution at 0.45A·cm $^{-2}$. (a), (b) is the distribution of the mass fraction of O_2 of CSFF and NDFF. (c), (d) is the distribution of partial pressure of O_2.

Fig.5 shows the distribution of oxygen mass fraction and partial pressure at the interface between the catalytic and diffusion layers with two different flow fields. For each flow field, the oxygen mass fraction along the flow direction exhibited a decreasing trend due to the continuous consumption in the oxygen reduction reaction [40]. Since the reaction gas cannot directly contact the gas diffusion layer, the oxygen concentration under the rib is much lower than that under the flow channel at the same horizontal position. A boundary probe of average value type is applied to the interface of the gas diffusion layer and the catalyst layer, and its expression is set as the oxygen mass fraction. In this way, the average oxygen mass fraction at the interface between the gas diffusion layer and the catalyst layer of the new 3D flow channel can be calculated to be 15.74%, which is higher than 13.4% of CSFF. The enhancement of mass transferability could be observed and could be attributed to the good structure of the combination of in-built blockage and trap-shape rib. As shown in Fig.5 (c) and (d), the

results of the oxygen partial pressure agree well with the distribution of the mass fraction of the oxygen, which further confirms the elevated oxygen mass transport resulting from the NDFF. Generally, oxygen flow in the flow channels is only in the in-plane direction. At the same time, the NDFF can introduce a velocity component direction in line with a concentration gradient, forming through-plane forced convection. In addition, the mass transfer under the rib can be greatly improved by the NDFF with more area where the reactant gas can directly contact the gas diffusion layer. Consequently, oxygen transport in membrane electrode assembly is enhanced.

Uneven distribution of reactant gas will result in uneven distribution of current density [44]. This is bad for the performance and the lifetime of a fuel cell [45]. Therefore, it is of great importance to improve the uniformity of reaction gas [46]. The variance was introduced to describe the oxygen distribution [31] and was exhibited in Fig.6. The oxygen consumption rate accelerates with increasing working current density, and the non-uniformity improves [47]. More importantly, the variance of the oxygen fraction of oxygen at the initial current density is reduced by 32.69%, and so is its growth rate, 20.15%, because the NDFF improved the mass transfer capacity.

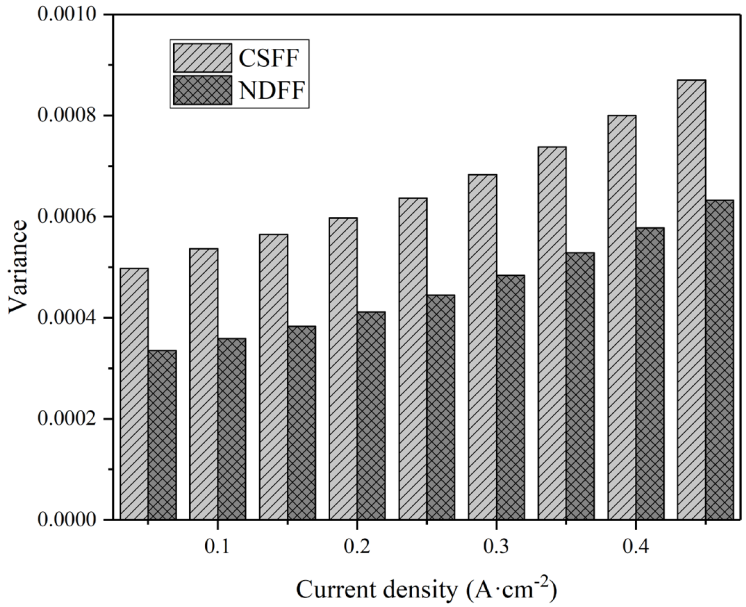

Figure 6. The variance of mass fraction of oxygen at the different working current density

Fig.7 shows the local fluctuation of the oxygen mass fraction along the flow direction at the cathode CL-GDL interface. The data in the figure is calculated from three positions: locate horizontally at the edge, middle at the cathode CL-GDL interface, and the area between these two sites. The NDFF produces a new working condition where the oxygen fraction changes periodically. At the same time, the CSFF does not have the periodic characteristics duo to its fixed channel height and rib shape. As shown in Fig.7, the highest oxygen mass fraction occurred at the middle of the interface, and it decreased gradually along the edge. The average oxygen mass fraction of the CSFF line2 decreased by 11.47% compared with line1. When the calculation position further moved away from the center area, the declined rate increased, and the difference of the average oxygen mass fraction between line2 and line3 was 22.64%.

It should be noted that the oxygen mass fraction at the same position of the NDFF is much higher than that of the CSFF. Furthermore, the attenuation rate also becomes

smaller, only 6.41% and 11.18%, respectively. The above results further confirm that the innovative design of the NDFF not only benefits oxygen transport from the channel to the MEA but also improves its distribution uniformity.

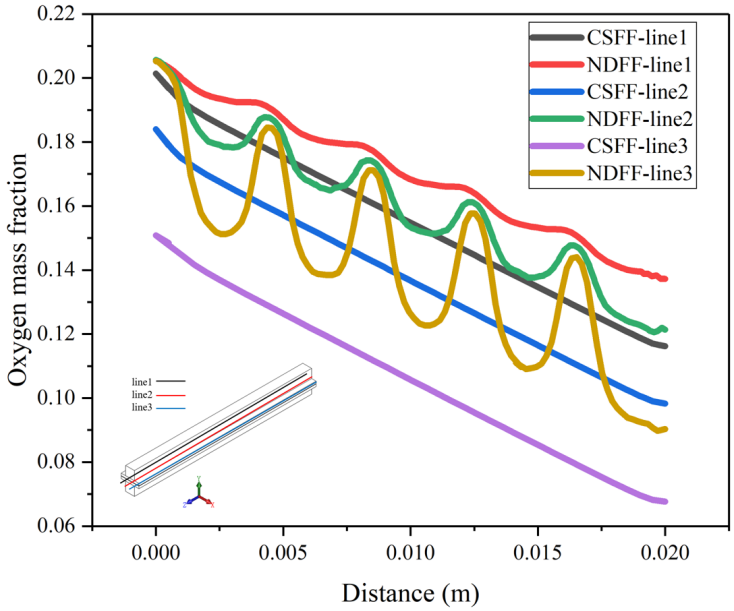

Figure 7: Local oxygen mass fraction fluctuation along the flow direction

4.3 Velocity distribution and effective mass transfer coefficient

In addition to the trap-shape rib design that allows more oxygen to diffusion into the MEA, another reasonable explanation for the enhanced mass transfer of the NDFF is that the flow channel with built-in obstacles can force the reaction gas to flow in the mass transfer direction. The contour of the velocity distribution can intuitively explain this phenomenon. As shown in Fig.8, the speed of the NDFF exhibits periodic changes and is 4 times as faster as that of the CSFF at the y-direction of the cathode CL-GDL interface. The CSFF rarely has flow at the y-direction, which means that the only way for oxygen to transfer into MEA is diffusion generated by the concentration gradient. It clarifies that the NDFF transformed the traditional diffusion into the optimized combination of diffusion and forced convection, and thus the mass transfer capacity

was considerably enhanced.

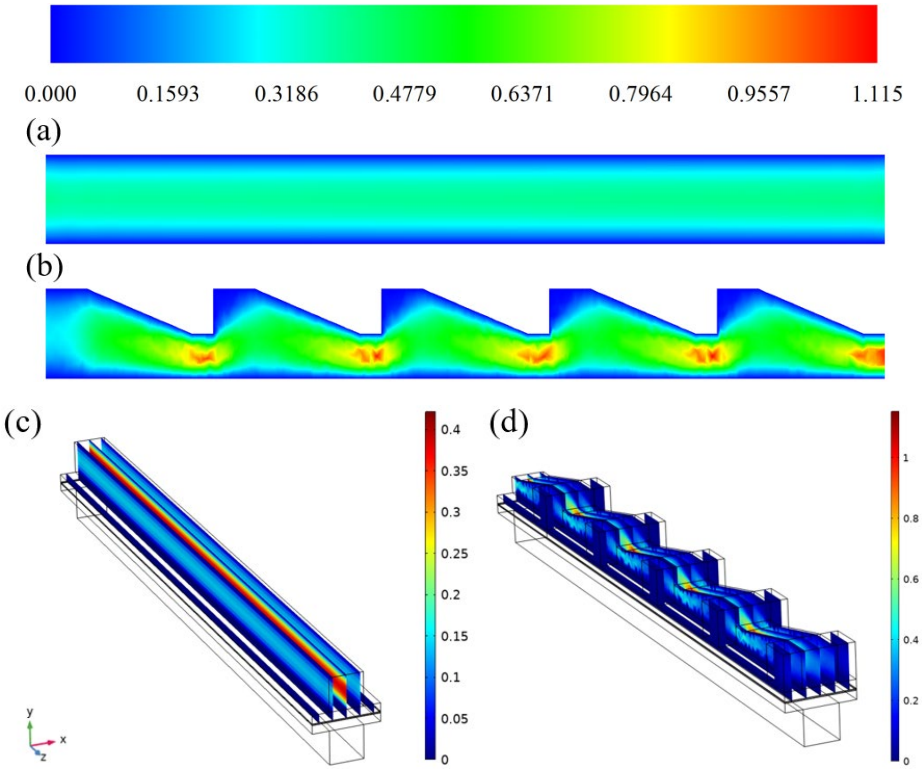

Figure 8: Velocity distribution of the cross section (x=1[mm]) (a)CSFF; (b)NDFF and the 3D contours (c)CSFF; (d)NDFF of the cathode flow channel.

To quantitatively evaluate the above phenomenon, effective mass transfer coefficient (EMTC), as shown in Equation (15), was proposed by [28] as an evaluation criterion for flow channel design of a fuel cell [10, 48].

$$\mathrm{EMTC} = \left| v \frac{\partial c_{loc,O_2}}{\partial y} \right| \tag{15}$$

Under the same working current density, the larger the EMTC, the superior mass transfer capacity, and the better the performance. As shown in Fig.9, the EMTC of the NDFF is two orders higher than that of the CSFF, which confirms that the NDFF's excellent structure can improve the mass transfer and performance. In addition, the EMTC increased with the improved working current density because more oxygen is

consumed, and a higher concentration gradient occurred. Finally, the EMTC of the NDFF at 0.4 A·cm^{-2} is 3.74 times bigger than that at 0.2 A·cm^{-2}, indicating that there is a higher demand for mass transfer rate.

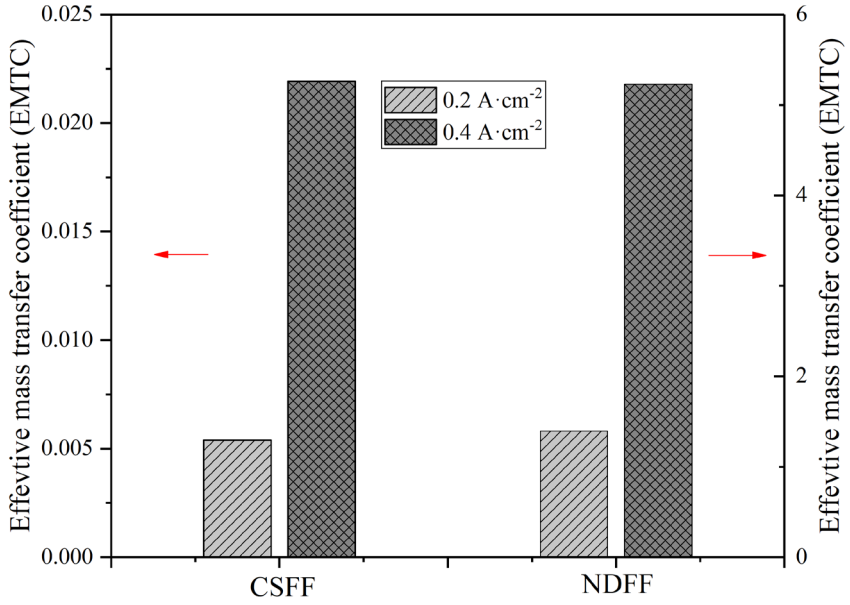

Figure 9: EMTC with two different flow fields

4.4 Water distribution

Water accumulation in a fuel cell has adverse influences, and it is essential to know the water distribution inside the fuel cell and reduce its total content [49]. Although the working condition that the gaseous water condensing into liquid water is not considered in this model, its trend can be quantitatively analyzed [27]. Fig.10 presents the water and relative humidity distribution at the cathode CL-GDL interface for two flow fields. As the oxygen reduction reaction produces water, the water mass fraction steadily increases along the direction of the flow channel from inlet to outlet. And the reaction gas which was unsaturated at the inlet quickly reaches a saturated state. There are many areas where the relative humidity of reaction gas is greater than 1. The water mass fraction of the NDFF is much lower than that of the CSFF. Moreover, its water

distribution is more uniform, eliminating the serious local flooding at the flow channel outlet. These results suggest that NDFF is a superior flow field for water management. For NDFF, the designed flow channel structures with in-built blockage and trap-shape rib can induce periodic changes in local velocity, local flow, and local pressure, which strengthen or arouse forced convection to enhance water removal.

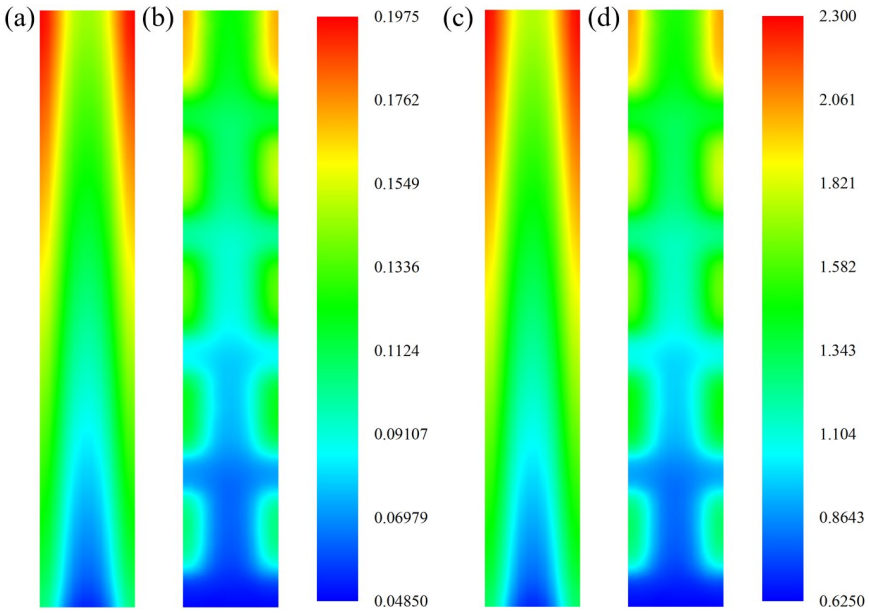

Figure 10: Distribution of water mass fraction and relative humidity at 0.45A·cm^{-2}. (a), (b) is the distribution of the mass fraction of H_2O of CSFF and NDFF. (c), (d) is the distribution of relative humidity of CSFF and NDFF.

4.5 Experimental loading performance

Fig.11 shows the comparison of experimental polarization curves for different flow fields under the same working conditions. There is an increased performance difference with the simulation results compared. Mass transfer and water management can both be improved by the NDFF. The calculated voltage increment of the NDFF is 0.08V at 0.45A·cm^{-2} while it is 0.21V according to experimental results. This can be attributed to the assumption that water inside PEMFCs is all gaseous. In an actual experiment,

flooding occurred in the flow channel of the CSFF due to its poor water management, and the performance difference of the CSFF between the simulation result and the experimental result is 0.24V while it is 0.11V for NDFF. Therefore, two aspects should be considered to give a reasonable explanation for the experimental 0.21V voltage increment of the NDFF. On the one hand, there is an increment of 0.08V for enhanced mass transfer. On the other hand, there is an increment of 0.13V for improved water management. These results are consistent with the trend obtained from the numerical model.

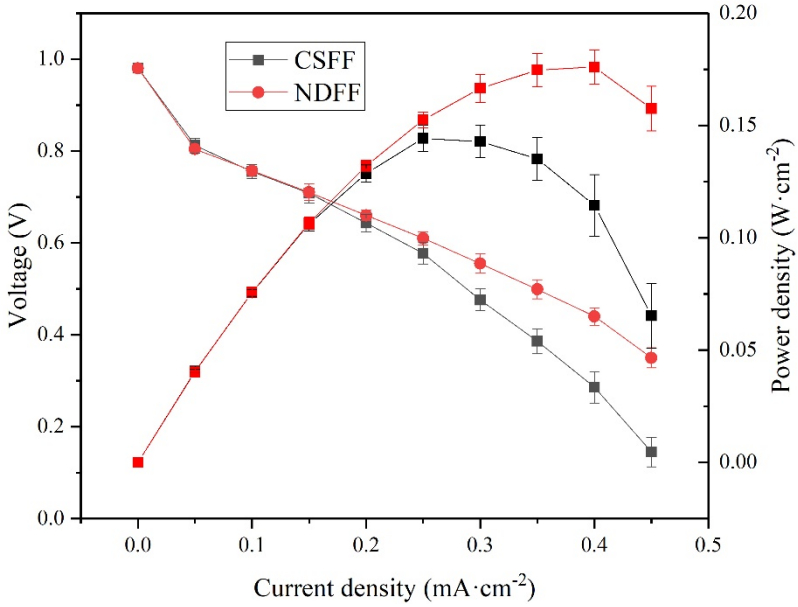

Figure 11: Comparison of experimental polarization curves for different flow fields.

Increasing the initial oxygen concentration in a fuel cell, such as the pre-supply strategy, effectively improves its dynamic performance [50]. The NDFF enables the higher initial oxygen mass fraction in the MEA and the higher total oxygen content due to the unique rib structure. Meanwhile, it also has a faster flow velocity [23]. Therefore, it can respond in a timelier manner during the loading process and exhibits better performance,

as described in Fig.12. The initial response voltage of the NDFF increased by 0.16V. And the NDFF shows better operation stability and less fluctuation in the continuous operation process after the fuel cell is loaded. This is because the NDFF has better water management and can discharge more quickly the generated water during the operation, alleviating the impacts of liquid water blocking the pores. The tested total polarization resistance is reduced by 12.97mΩ with CSFF compared.

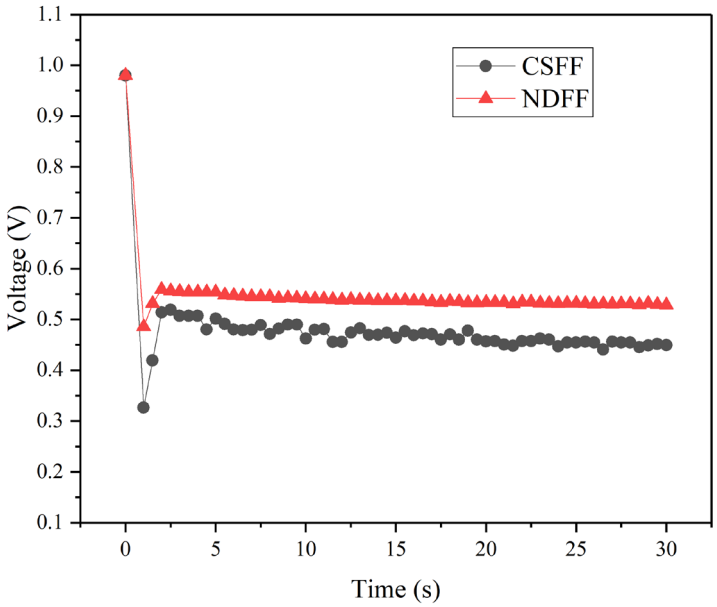

Figure 12: Dynamic response of PEMFCs with different flow fields

4.6 Pressure distribution and energy efficiency ratio

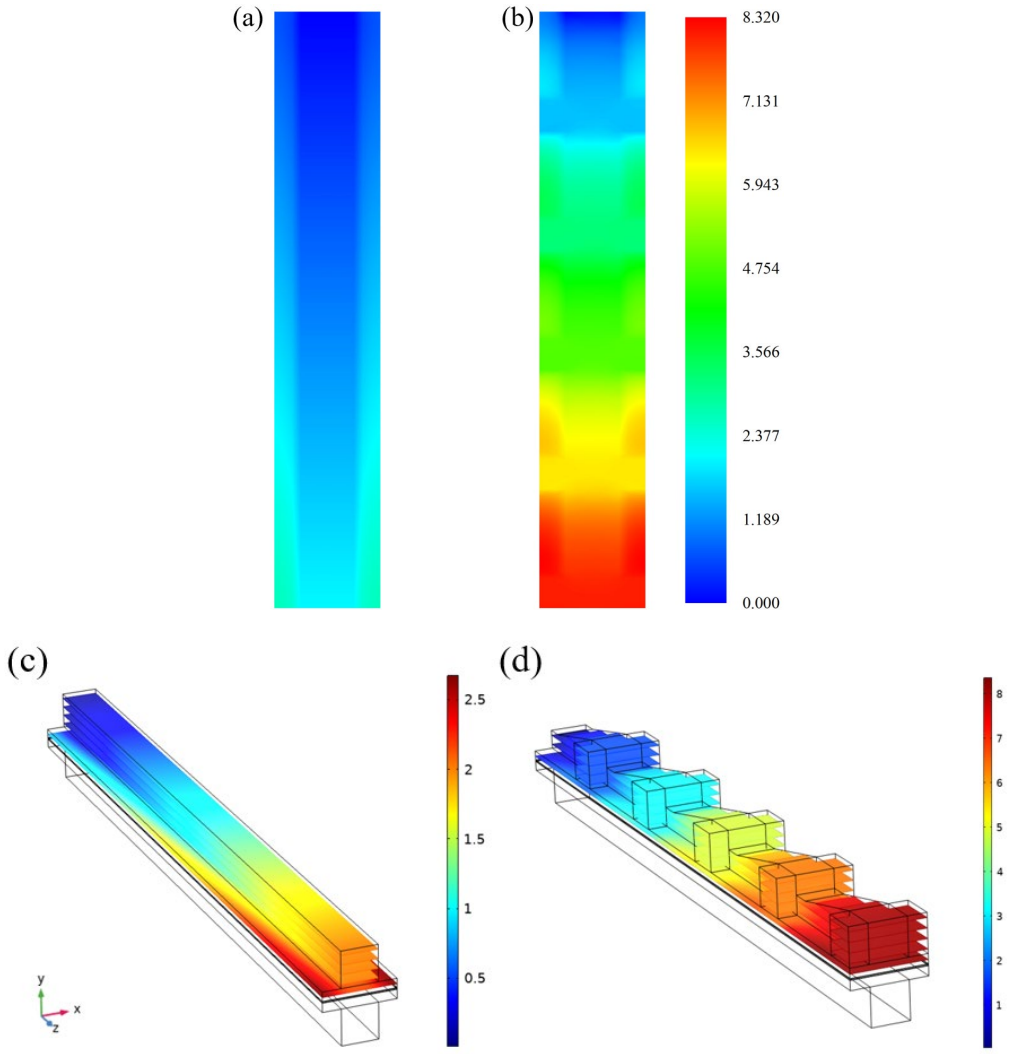

Figure 13: Pressure distribution at the cathode CL-GDL (a)CSFF; (b)NDFF and the 3D contours (c)CSFF; (d)NDFF of the cathode flow channel.

Fig.13 shows the pressure distribution at the cathode CL-GDL. There is a tiny pressure drop for the CSFF. Therefore, the parasitic power of the CSFF is very small, and its structure optimization has crucial practical value [48]. Compared with CSFF, the pressure distribution of the NDFF presents periodic characteristics. Due to the increase of the fluid disturbance, the pressure drops, and the parasitic power increases simultaneously. It is necessary to comprehensively evaluate the relationship between the parasitic power and the output power after the flow field structure changes and the

proposed energy efficiency ratio as shown in Equation (16):

$$\mathrm{EER} = \frac{J\Delta V}{\Delta(\Delta P\overline{u}A_{ch})} \tag{16}$$

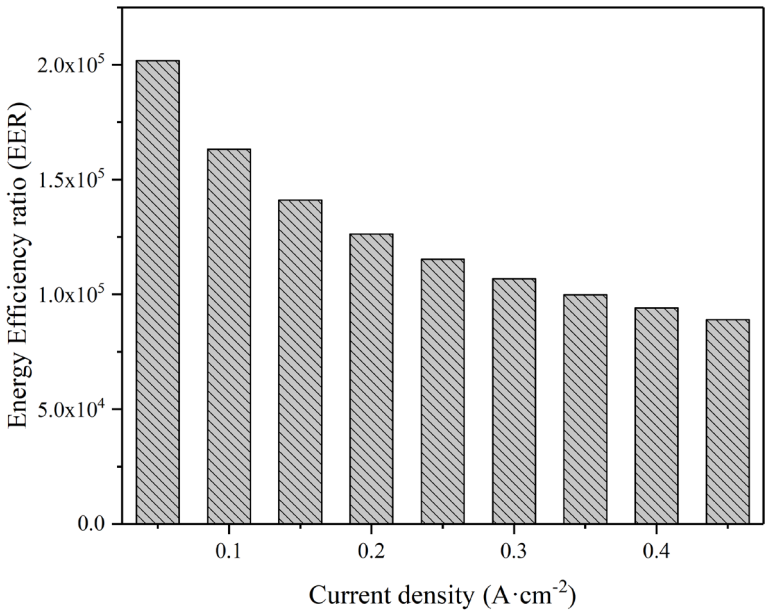

Figure 14: EER of the NDFF compared with CSFF

$\Delta P\overline{u}A_{ch}$ can be used to calculate the parasitic power loss caused by the reaction gas flowing in the fuel cell [10]. The product of the working current J and the working voltage V represent the output power of the fuel cell. Based on the above results, the Energy Efficiency Ratio (EER) is proposed to quantitatively evaluate the effects of the flow channel change on the overall performance of the fuel cell. It is defined as the ratio of the difference of the output power and parasitic power between two flow fields, as shown in Equation (16). The increased output power due to the changes in the flow field is greater than the increased parasitic power when the EER is bigger than 1, and such an improvement of the flow field will help improve the overall performance of the fuel cell. Fig.14 shows the EER of the NDFF compared with the CSFF. The EER decreases with the increased current density as more reaction gas increases the gas flow disturbance. However, the EER is always far greater than 1, indicating that the NDFF

can improve the fuel cell's net power.

5 Conclusion

In this paper, a combination of numerical simulation and experiment is used to study the performance improvement and internal mechanism of the new 3D flow field compared to the traditional straight flow field. The main results obtained are as follows:

1) The average oxygen mass fraction of the new 3D flow field at the interface between the catalyst layer and the gas diffusion layer is 15.74%, which is higher than the 13.4% of the traditional straight flow channel. The effective mass transfer coefficient analysis shows that the new 3D flow field can optimize the traditional diffusion mass transfer method to a combination of diffusion and convection mass transfer, thereby greatly enhancing the mass transfer performance.

2) The distribution variance of the initial current density of the new 3D flow field is reduced by 32.69%, and with the increase of the current density, its distribution variance growth rate is also reduced by 20.15%. This is because the new 3D flow field can significantly improve the ridge mass transfer to improve the uniformity of oxygen distribution.

3) The maximum value of water mass fraction in the new 3D flow field is reduced by 13.51% compared with the traditional straight flow channel. The new 3D flow field can cause periodic changes in speed, direction, and pressure, and strengthen the purge of moisture inside the PEMFC, thereby strengthening the water management of the PEMFC.

4) Compared with the straight flow field, the experimental result shows that the voltage

of the new 3D flow field at 0.45A·cm^{-2} increases by 0.205V. The performance difference between the simulation result and the experimental result of the straight flow field is 0.23611V, and that of the new 3D flow field is 0.10778V. The difference between the two is 0.12833V, which is because different flow fields have different water management capabilities. In summary, the performance increase of 0.205V obtained through the new 3D flow field experiment can be analyzed from two aspects, which are the increase of 0.07647V due to the enhanced mass transfer and the increase of 0.12833V due to the optimization of water management. The results are consistent with the simulation results that the new 3D flow channel can enhance mass transfer and water management.

5) The dynamic response capability and stable operation capability of the new 3D flow field are better than the traditional straight flow channel. This is because the new 3D flow field has a higher initial oxygen content, faster reaction gas flow rate, and better water management capabilities.

6) The energy efficiency ratio of the new 3D flow channel is far greater than 1, indicating that it can increase the net power output of the PEMFC. The energy efficiency ratio is defined as the ratio between the difference in output performance before and after the optimization of the flow channel structure and the difference in parasitic power loss. The energy efficiency ratio is greater than 1, indicating that the net output of the PEMFC can be increased.

Acknowledgments

This work was supported by the National Key Research and Development Program of

China (No.2018YFC0810000), the National Natural Science Foundation of China (No. 51776144), Natural Science Foundation of Hubei Province (No. 2020CFA040) and Wuhan Applied Foundational Frontier Project (No. 2020010601012205).

References

[1] Selem SI, Hasanien HM, El-Fergany AA. Parameters extraction of PEMFC's model using manta rays foraging optimizer. Int. J. Energy Res. 2020;44(6):4629-4640.

[2] Chabane D, Iqbal M, Harel F, et al. Coupling a metal hydride tank with a PEMFC for vehicular applications: A simulations framework. Int. J. Energy Res. 2021;45(11):16511-16523.

[3] Shen J, Tu Z, Chan SH. Effect of gas purging on the performance of a proton exchange membrane fuel cell with deadended anode and cathode. Int. J. Energy Res. 2021;45(10):14813-14823.

[4] Wang, JY. Barriers of scaling-up fuel cells: Cost, durability and reliability. Energy. 2015;80: 509-521.

[5] Wang YL, Si C, Qin YZ, Wang XD, et al. Bio-inspired design of an auxiliary fishbone-shaped cathode flow field pattern for polymer electrolyte membrane fuel cells. Energy Convers Manag. 2021;227: 113588.

[6] Shin DK, Yoo JH, Kang DG, Kim MS. Effect of cell size in metal foam inserted to the air channel of polymer electrolyte membrane fuel cell for high performance. Renew Energ. 2018; 115: 663-675.

[7] Jiao K, Xuan J, Du Q, Bao ZM, et al. Designing the next generation of proton-exchange membrane fuel cells. Nature. 2021; 595(7867): 361-369.

[8] Ghanbarian A, Kermani MJ. Enhancement of PEM fuel cell performance by flow channel indentation. Energy Convers Manag. 2016; 110: 356-366.

[9] Tiss F, Chouikh R, Guizani A, A numerical investigation of reactant transport in a PEM fuel cell with partially blocked gas channels. Energy Convers Manag. 2014; 80: 32-38.

[10] Shen J, Tu Z, Chan SH, Enhancement of mass transfer in a proton exchange membrane fuel cell with blockage in the flow channel. Appl Therm Eng, 2019; 149: 1408-1418.

[11] Fahruddin A, Ichsani D, Taufany F, Widodo BUK, Widodo WA. The effect of blockage shape on the performance of a polymer electrolyte membrane fuel cell with a biometric flow field. Int J Hydrogen Energy. 2021;46(8): 6028-6036.

[12] Rezazadeh S, Ahmadi N. Numerical investigation of gas channel shape effect on proton exchange membrane fuel cell performance. J Braz. Soc. Mech. Sci. Eng. 2015, 37:789-802

[13] Kang DG, Lee DK, Choi JM, Shin DK, et al., Study on the metal foam flow field with porosity gradient in the polymer electrolyte membrane fuel cell. Renew Energ. 2020; 156: 931-941.

[14] Shen J, Xu L, Chang HW, Tu Z, Chan SH, Partial flooding and its effect on the performance of a proton exchange membrane fuel cell. Energy Convers Manag, 2020; 207: 112537.

[15] Chen B, Wang M, Tu Z, Gong X, et al., Moisture dehumidification and its application to a 3 kW proton exchange membrane fuel cell stack. Int J Hydrogen Energy.

2015; 40(2): 1137-1144.

[16] Cooper NJ, Santamaria AD, Becton MK, Park JW, Investigation of the performance improvement in decreasing aspect ratio interdigitated flow field PEMFCs. Energy Convers Manag, 2017;136: 307-317.

[17] Liu HC, Cheng LS, Yang WM, Enhanced water removal performance of a slope turn in the serpentine flow channel for proton exchange membrane fuel cells. Energy Convers Manag. 2018;176: 227-235.

[18] Baik KD, Seo IS, Metallic bipolar plate with a multi-hole structure in the rib regions for polymer electrolyte membrane fuel cells. Appl Energy. 2018;212: 333-339.

[19] Huang HZ, Lei H, Liu MX, Wang TY, Effect of superior mesenteric artery branch structure-based flow field on PEMFC performance. Energy Convers Manag, 2020;226: 113546.

[20] Wang YL, Wang SX, Wang GZ, Yue L, Numerical study of a new cathode flow-field design with a sub-channel for a parallel flow-field polymer electrolyte membrane fuel cell. Int J Hydrogen Energy. 2018;43(4): 2359-2368.

[21] Huang Z, Xing L, Tu Z. Load changing characteristics of the hydrogen-air and hydrogen-oxygen proton exchange membrane fuel cells. Int J Energy Res. 2021;1-13.

[22] Yan QG, Toghiani H, Causey H, Steady state and dynamic performance of proton exchange membrane fuel cells (PEMFCs) under various operating conditions and load changes. J Power Sources. 2006;161(1): 492-502.

[23] Kim S, Shimpalee S, Van Zee JW, Effect of Flow Field Design and Voltage Change Range on the Dynamic Behavior of PEMFCs. J Electrochem Soc. 2005;152(6):

1265.

[24] Yan W, Li H, Weng W. Transient mass transport and cell performance of a PEM fuel cell. Int J Heat Mass Tran. 2017;107: 646-656.

[25] Heidary H, Kermani MJ, Dabir B, Influences of bipolar plate channel blockages on PEM fuel cell performances. Energy Convers Manag. 2016;124: 51-60.

[26] Lim BH, Majlan EH, Daud WRW, Rosli MI, Husaini T. Numerical analysis of modified parallel flow field designs for fuel cells. Int J Hydrogen Energy 2017;42(14): 9210-9218.

[27] Li WK, Zhang QL, Wang C, Yan XH, et al.. Experimental and numerical analysis of a three-dimensional flow field for PEMFCs. Appl Energy. 2017;195: 278-288.

[28] Cai YH, Fang Z, Chen B, Yang TQ, et al.. Numerical study on a novel 3D cathode flow field and evaluation criteria for the PEM fuel cell design. Energy. 2018; 161: 28-37.

[29] Min C, He J, Wang K, Xie LY, Yang XG. A comprehensive analysis of secondary flow effects on the performance of PEMFCs with modified serpentine flow fields. Energy Convers Manag. 2019;180: 1217-1224.

[30] Cai YH, Wu D, Sun JM, Chen B. The effect of cathode channel blockages on the enhanced mass transfer and performance of PEMFC. Energy. 2021;222: 119951.

[31] Chen HC, Zhao X, Qu BW, Zhang T, et al.. An evaluation method of gas distribution quality in dynamic process of proton exchange membrane fuel cell. Appl Energy. 2018;232: 26-35.

[32] Behrou R, Pizzolato A, Forner-Cuenca A. Topology optimization as a powerful tool to design advanced PEMFCs flow fields. Int J Heat Mass Tran. 2019;135: 72-92.

[33] Zhang Y, Tao YK, Shao J. Application of porous materials for the flow field in polymer electrolyte membrane fuel cells. J Power Sources. 2021;492: 229664.

[34] Ubong EU, Shi Z, Wang X. Three-dimensional modeling and experimental study of a high temperature PBI-based PEM fuel cell. J Electrochem Soc. 2009;156(10): B1276.

[35] Chowdhury MZ, Timurkutluk B. Transport phenomena of convergent and divergent serpentine flow fields for PEMFC. Energy. 2018;161: 104-117.

[36] Meng H, A two-phase non-isothermal mixed-domain PEM fuel cell model and its application to two-dimensional simulations. J Power Sources. 2007;168(1): 218-228.

[37] Thomas S, Bates A, Park Sam, Sahu AK, et al., An experimental and simulation study of novel channel designs for open-cathode high-temperature polymer electrolyte membrane fuel cells. Appl Energy. 2016;165: 765-776.

[38] Bao C, Bessler WG. Two-dimensional modeling of a polymer electrolyte membrane fuel cell with long flow channel. Part I. Model development. J Power Sources. 2015;275: 922-934.

[39] Yuan W, Tang Y, Pan MQ, Li ZT, et al.. Model prediction of effects of operating parameters on proton exchange membrane fuel cell performance. Renew Energ. 2010;35(3): 656-666.

[40] Zhang SY, Qu ZG, Xu HT, Talkhoncheh FK, et al.. A numerical study on the

performance of PEMFC with wedge-shaped fins in the cathode channel. Int J Hydrogen Energy. 2021;46(54): 27700-27708.

[41] Le AD, Zhou B. A general model of proton exchange membrane fuel cell. J Power Sources. 2008;182(1): 197-222.

[42] Meng K, Zhou HR, Chen B, Tu Z. Dynamic current cycles effect on the degradation characteristic of a H2/O2 proton exchange membrane fuel cell. Energy. 2021;224: 120168.

[43] Barbir F. PEM fuel cells: theory and practice. 2013: Academic Press.

[44] Huang Z, Tu Z. Local current density distribution of proton exchange membrane fuel cell and its research prospects. Prog Chem. 2020;32(07): 943-949.

[45] Albaghdadi M, Aljanabi H. Effect of operating parameters on the hygro–thermal stresses in proton exchange membranes of fuel cells. Int J Hydrogen Energy. 2007;32(17): 4510-4522.

[46] Su GQ, Yang DJ, Xiao QF, Dai HQ, et al.. Effects of vortexes in feed header on air flow distribution of PEMFC stack: CFD simulation and optimization for better uniformity. Renew Energ. 2021;173: 498-506.

[47] Chen HC, Liu B, Zhang T, Pei PC. Influencing sensitivities of critical operating parameters on PEMFC output performance and gas distribution quality under different electrical load conditions. Appl Energy. 2019;255: 113849.

[48] Shen J, Tu Z, Chan SH. Evaluation criterion of different flow field patterns in a proton exchange membrane fuel cell. Energy Convers Manag. 2020; 213: 112841.

[49] Yue L, Wang SX, Araki T, Utaka Y, et al. Effect of water distribution in gas

diffusion layer on proton exchange membrane fuel cell performance. Int J Hydrogen Energy. 2021;46(3): 2969-2977.

[50] Shen Q, Hou M, Yan XQ, Liang D, et al. The voltage characteristics of proton exchange membrane fuel cell (PEMFC) under steady and transient states. J Power Sources. 2008;179(1): 292-296.

Nomenclature

A_c	Tafel slope, V
c	Species concentration, mol/m^3
D_{ij}	Diffusion coefficient, m^2/s
F	Faraday constant, C/mol
i	Working current density, A/m^2
i_0	Exchange current density, A/m^2
M	Molecular mass, kg/mol
p	Working pressure, Pa
R	Universal gas constant, J/(mol·K)
S	Source term
T	Working temperature, K
u	Velocity, m/s
x	Mole fraction

Greek symbols

α	Charge transfer coefficient

ε	Porosity
η	Overpotential, V
μ	Dynamic viscosity, $N \cdot s/m^2$
ρ	Density, kg/m^3
σ	Electrical conductivity, S/m
φ^0	Electrode equilibrium potential, V
Φ	Phase potential, V
ω	Mass fraction

Subscript and superscript

a	Anode
c	Cathode
loc	Local
ref	Reference
eff	effectiveness
i, k	Species
s	Electrode phase
l	Electrolyte phase